Journal of Materials Chemistry C

ROYAL SOCIETY OF CHEMISTRY

COMMUNICATION

View Article Online
View Journal | View Issue

Cite this: J. Mater. Chem. C, 2024, 12, 3053

Received 4th January 2024,
Accepted 12th February 2024

DOI: 10.1039/d4tc00039k

rsc.li/materials-c

Cubic and hexagonal boron nitride phases and phase boundaries†

Abhijit Biswas, *[a] Gustavo A. Alvarez,[b] Manoj Tripathi, *[c] Jonghoon Lee,[d] Tymofii S. Pieshkov,[ae] Chenxi Li,[a] Bin Gao,[f] Anand B. Puthirath,[a] Xiang Zhang,[a] Tia Gray,[a] Jacob Elkins,[a] Robert Vajtai,[a] Pengcheng Dai,[f] A. Glen Birdwell,[g] Mahesh R. Neupane,[g] Tony Ivanov,[g] Elias J. Garratt,[g] Bradford B. Pate,[h] Ajit K. Roy,[d] Alan Dalton, *[c] Zhiting Tian*[b] and Pulickel M. Ajayan*[a]

Phase stability of boron nitride (BN) polymorphs at elevated temperature is perplexing due to their complex nucleation and growth kinetics, nevertheless, holds great significance in fundamental science and technology. Therefore, the phase-transformation of three-dimensional cubic BN (3D c-BN) to a two-dimensional hexagonal BN (2D h-BN) or *vice versa*, remains an exciting domain to explore. Here, we used temperature-dependent spark plasma sintering on 3D c-BN, enabling phase transformations to a mixed phase of 3D/2D c-BN/h-BN material and ultimately to 2D h-BN. The phase transformed 2D h-BN ceramic features an extremely high density reaching ~90% of the theoretical limit, and exhibits excellent room temperature thermal conductivity and mechanical properties. Our findings provide valuable fundamental insights into the complex phase diagram, the relative stability regimes and boundaries of 3D c-BN and 2D h-BN phase, with the exhibition of functional properties, pivotal for extreme environments sustainable material-based technology.

Introduction

Polymorphs of boron nitride (BN) are unique ultrawide-bandgap materials showing a plethora of functional properties, including electrical insulations, elevated temperature oxidation and corrosion-resistant coatings, high mechanical strength, excellent radiation shielding and thermal conductivity.[1–4] These makes BN as a valuable material for applications in extreme environments across various industries including engineering, aerospace, electronics, energy and defense.[1–4] The most common polymorphs of BN are two-dimensional hexagonal boron nitride (2D h-BN) and three-dimensional cubic boron nitride (3D c-BN).[1,2] The 2D h-BN has a layered hexagonal crystal structure (a = 2.504 Å, c = 6.661Å) analogous to graphite.[2] It is the most stable polymorph of BN and possesses the lowest energetic orientation along the [002] plane. h-BN is an electrical insulator (band gap E_g ~5.9 eV), chemically inert, and possesses excellent thermal conductivity.[2] It is often used as a solid-state lubricant, for thermal management, and in high-temperature applications.[5] On the other hand, c-BN lattice has a cubic structure (a = 3.61 Å) and is analogous to diamond.[6–8] c-BN holds significant importance due to its exceptional properties and versatile applications in various industries. It is the most stable polymorphic form, and the lowest energetic facet is along [111].[9,10] The band gap of the cubic phase is higher (E_g of ~6.3 eV) than its 2D phase, which makes c-BN a better insulator than h-BN. c-BN is hard with Vickers hardness (H_v) ~62 GPa.[1] Therefore, due to its exceptional hardness c-BN holds significant importance as wear resistance, and useful as an abrasive for cutting tools, grinding wheels, crucibles, and drills.[3]

The elevated temperature stability and phase transformations of BN polymorphs are non-trivial and puzzling, and a clear understanding of their phase formation kinetics, and property evaluations is lacking.[11–22] It is well known that in ambient conditions, the most thermodynamically stable BN phase is h-BN, and at high-temperature and high-pressure (HTHP) it transforms into c-BN.[1,2] There has been a debate regarding the phase stabilization of c-BN; several reports claim it to be a metastable phase formed only under HTHP conditions.[8] However, several reports also suggest that c-BN is the most stable phase at ambient conditions, while the phase

[a] Department of Materials Science and Nanoengineering, Rice University, Houston, TX, 77005, USA. E-mail: 01abhijit@gmail.com, ajayan@rice.edu
[b] Sibley School of Mechanical and Aerospace Engineering, Cornell University, Ithaca, NY 14853, USA. E-mail: zhiting@cornell.edu
[c] Department of Physics and Astronomy, University of Sussex, Brighton BN1 9RH, UK. E-mail: m.tripathi@sussex.ac.uk, A.B.Dalton@sussex.ac.uk
[d] Air Force Research Laboratory, Materials and Manufacturing Directorate, WPAFB, OH, 45431, USA
[e] Applied Physics Graduate Program, Smalley-Curl Institute, Rice University, Houston, TX, 77005, USA
[f] Department of Physics and Astronomy, Rice University, Houston, TX, 77005, USA
[g] DEVCOM Army Research Laboratory, RF Devices and Circuits, Adelphi, Maryland 20783, USA
[h] Naval Research Laboratory, Washington, DC 20375, USA

† Electronic supplementary information (ESI) available: Supplementary materials contain HRTEM, EDS mapping, XRD, FESEM, Raman spectroscopy, FTIR characterizations, and laser flash results and elastic indentation depth map of BN. See DOI: https://doi.org/10.1039/d4tc00039k

transformation (c-BN → h-BN) could occurs due to the complex thermodynamics, growth kinetics, grain size variations and impurities.[13–21] Therefore, experimental exploration and comprehensive understanding of the HTHP stable phases of BN is important and relevant for extreme conditions applications.[23] Different phases of BN have diverse properties, and being able to control/tune their phase formation allows the designing of BN based materials and composites with specific characteristics for various applications.[3,4,24–30] Accordingly, experimental investigation of BN phase stability and phase transformations remain an exciting area of unexplored/challenging field of research, with the observations of novel functionalities.

Here, we explored the temperature-dependent phase evolution of bulk 3D c-BN by using the spark plasma sintering (SPS) process. With the increase in SPS temperature, we observed that 3D c-BN transforms to mixed-phase 2D/3D c-BN/h-BN material and finally to 2D h-BN. Moreover, the transformed h-BN ceramic exhibits excellent thermal conductivity and Young's modulus, with achieved ∼90% theoretical density of h-BN. These findings hold great potential in advancing our fundamental understanding of BN's phase diagram at elevated temperatures and in exploring the potential applications of dense and hard h-BN in extreme condition technology.

Results and discussion

Structural, chemical, and microscopic characterizations

The investigation begins with the validation of phases through comprehensive characterization of as received c-BN powder by using various techniques, such as X-ray diffraction (XRD), X-ray photoelectron spectroscopy (XPS), field-emission scanning electron microscope (FESEM), Raman spectroscopy, and Fourier-transform infrared spectroscopy (FTIR), which shows all the characteristics features of c-BN (Fig. 1, left panel). For instance, XRD shows the clear and sharp (111) peak, which is the most stable facet of c-BN, along with other diffraction peaks (Fig. 1a).[31–33] XPS shows the B–N bonding related peaks (Fig. 1b). In the XPS c-BN does not show π-Plasmon peaks (at ∼9 eV apart from the main B–N peak), a key feature distinguishing c-BN from h-BN (Fig. 1b).[31,34] FESEM demonstrated the 3D particle-like morphology with particle sizes of 1–2 μm (Fig. 1c). In Raman spectra, c-BN exhibited two sharp peaks at ∼1054 cm^{-1} (transverse optical, [TO]) and at ∼1304 cm^{-1} (longitudinal optical, [LO]) (Fig. 1d).[32,35] The FTIR of c-BN shows a characteristic TO peak at ∼1054 cm^{-1} (Fig. 1e). The primary bonding in c-BN is predominantly covalent, with a slight ionic character, which indicates the presence of both LO and TO phonon modes in the Raman spectra.[32] The intensity of LO and TO Raman modes is also correlated with the orientation of c-BN, because it is revealed that (111) plane-oriented c-BN shows a stronger TO peak than LO.[32]

For the powdered c-BN, we also observed a similar feature consistent with the observation of intense (111) peaks in XRD. Furthermore, we performed High-angle annular dark-field scanning transmission electron microscopy (HAADF-STEM) showing crystals with sharp edges (Fig. S1, ESI†). Energy dispersive spectrum (EDS) mapping shows a uniform distribution of B and N elements indicating the homogeneity with a B : N ratio of ∼1 : 1 (precisely 51.16 : 48.69). All of these observations confirm the predominantly (111) oriented c-BN, with particle sizes of ∼1–2 μm.

We conducted SPS, a high-temperature pressure self-densification process, on c-BN powders at various temperatures, ranging from room temperature up to the maximum achievable elevated temperature of 2200 °C, while maintaining a pressure of 90 MPa. Up to the temperature of 1250 °C, c-BN phase remained unchanged (Fig. S2–S4, ESI†). As the temperature increased to 1500 °C, we observed its susceptibility to changes (Fig. 1, right panel). To analyze the c-BN after SPS sintering, we again employed XRD, XPS, FESEM, Raman spectroscopy, and FTIR spectroscopy. The XRD results although only showed c-BN related peaks, but interestingly, the surface sensitive XPS analysis revealed the presence of π-plasmon peaks related to h-BN (Fig. 1b, inset, right panel), which were not present in the pristine c-BN case.[31,34] Moreover, the Raman peaks intensities of c-BN also became significantly weaker, whereas FTIR exhibited a clear h-BN related infrared (IR) active vibrational phonon mode at ∼1385 cm^{-1} (in-plane stretching).[36] The volume fraction of the c-BN or h-BN content in BN is many cases are estimated from FTIR.[31,32,37] Lower FTIR intensity of h-BN peaks indicates a small fraction of h-BN contained in c-BN. These characterizations of the c-BN powder after SPS at 1500 °C and 90 MPa thus indicate its predominantly cubic phase (c-BN), with some traces of the hexagonal phase (h-BN), implying BN's overall mixed-phase configuration.

The high-resolution transmission electron microscopy (HRTEM) images revealed a mixed phase of the sample as well. Fig. 2a shows a TEM image of two particles, c-BN and the h-BN, which varies from 0.45 μm to 1.8 μm after one-hour sonication, consistent with the FESEM (Fig. 1c). The atomically resolved arrangement of the particles validates their respective phases as follows: cubical for c-BN and hexagonal for h-BN. The magnified image of the region of interest (ROI) (Fig. 2b, red square) with overlapped c- and h-BN areas and atomic resolution TEM image of c-BN lattice (Fig. 2b, white dashed square) is shown in Fig. 2c. Because the h-BN particle was considerably thicker than the c-BN particle, getting a good atomic resolution image from TEM was not trivial. However, the difference in phases is apparent by analyzing the selected area electron diffraction (SAED) images (Fig. 2d and e). The SAED aperture limited the exposure area to the circles labelled 1 and 2 (Fig. 2a). By measuring the angles and distance ratios between diffraction spots, we could compare them with simulated results (Fig. 2f and g)[38] to determine the orientation of each particle. Region 1 shows (110) c-BN, whereas region 2 shows $(10\bar{1}0)$ h-BN. Therefore, HRTEM with SAED confirms the mixed phase nature of BN, after the SPS at 1500 °C and 90 MPa pressure.

Subsequently, we further increased the temperature, performed the SPS at 1700 °C and 90 MPa pressure for 1 hour, and characterized the sample with the techniques mentioned above for pre and post SPS treatment, (Fig. 3). The SPS treatment at

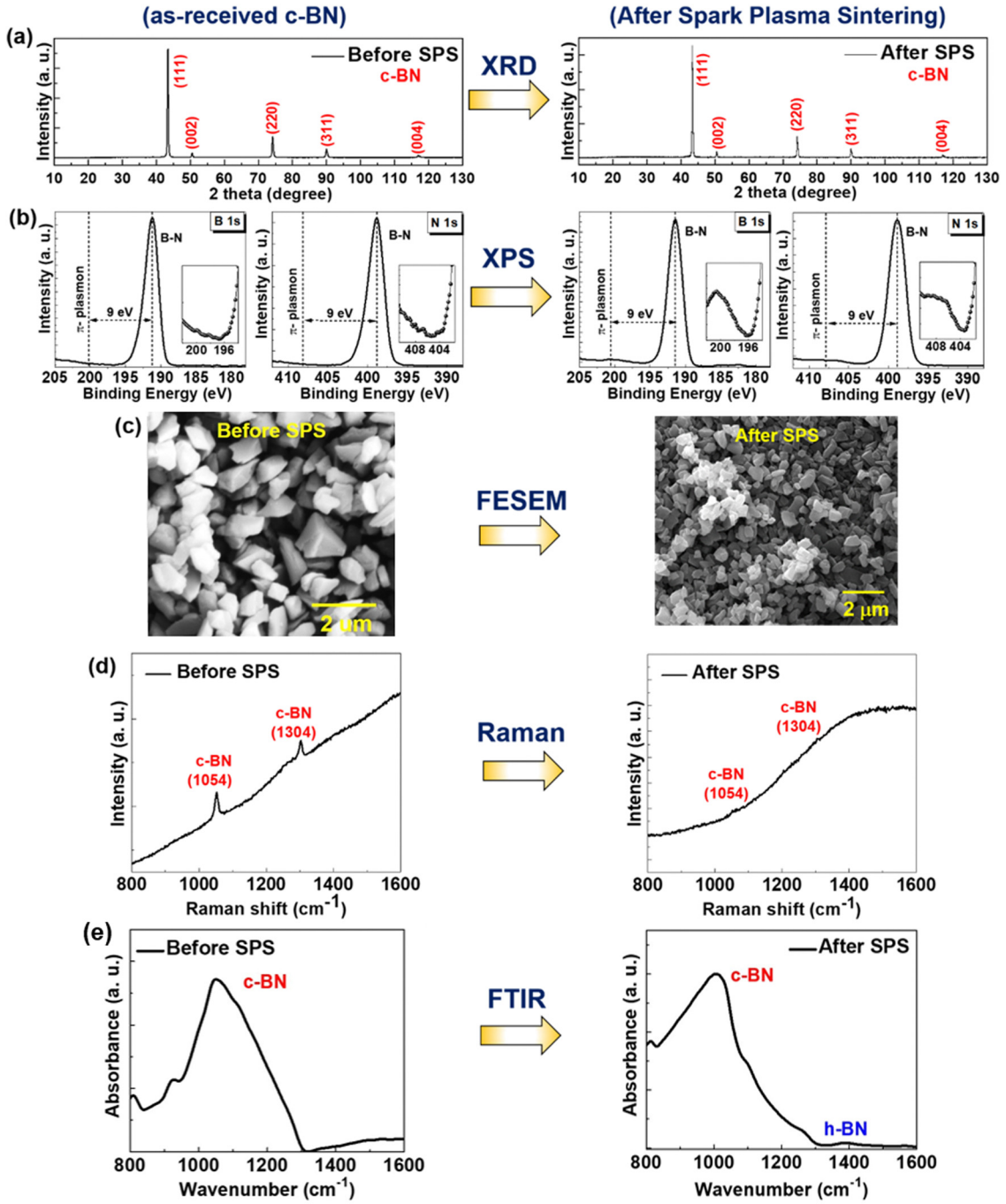

Fig. 1 Characterizations of c-BN, before and after the SPS at 1500 °C, and 90 MPa pressure. (a)–(e) XRD, XPS, FESEM, Raman spectroscopy, and FTIR spectra. Inset of XPS (right panel) (after the SPS) shows the plasmon peaks corresponding to h-BN. FTIR also shows the formation of mixed phase 3D/2D c-BN/h-BN, after the SPS.

1700 °C, we observed a phase transformation of 3D c-BN to 2D h-BN. XRD displayed the emergence of all peaks associated with h-BN, including the prominent (002) peak at ~26.5°.[36] In XPS analysis, clear π-plasmon peaks (separated by ~9 eV from the main peak) appeared alongside the B–N bonding peaks.[34] FESEM illustrated sheet-like features with lateral sizes ~5 µm. Raman spectra indicated only a peak at ~1367 cm^{-1}, corresponding to the symmetric in-plane stretching of B–N.[36]

In addition, FTIR revealed the presence of in-plane stretching TO vibration modes, characteristic of h-BN. Under the HRTEM and SAED image (Fig. S5, ESI†), $(10\bar{1}0)$ orientation of h-BN is observed from plane normal N(*hkl*). The inter-planar *d* spacing of the (002) plane is increased (~3.32 Å) (Fig. S6, ESI†), as compared with traditional h-BN (d_{002} ~3.30 Å).[36] Increased *d* spacing of (002) peak is usually found during the crystallization of h-BN.[39] Moreover, the density (ρ) of the sintered h-BN disk is

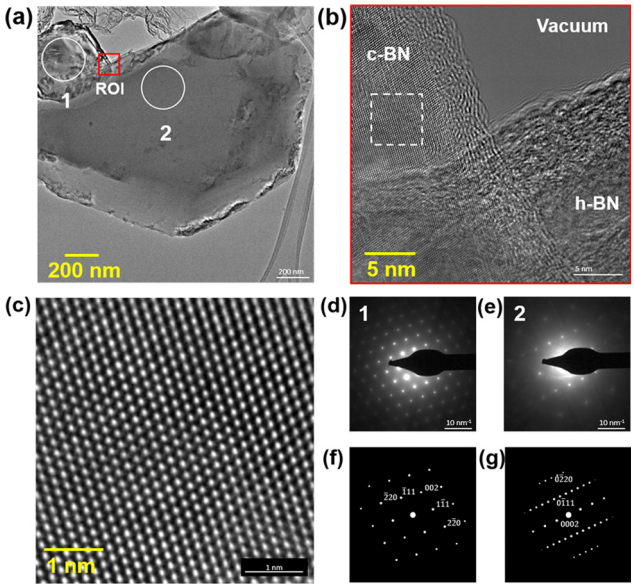

Fig. 2 HRTEM after the SPS at 1500 °C, and 90 MPa. (a) Overview TEM image of h-BN and c-BN particles. (b) High-resolution image of the region of interest (ROI) from (a) with c-BN particles on top of h-BN. (c) Magnified region of c-BN from (b) showing atomic resolution. (d) and (e) SAED patterns taken from areas 1 and 2 marked on (a), denoting regions of c-BN and h-BN. (f) and (g) Simulated diffraction patterns of (110) c-BN and (10$\bar{1}$0) h-BN, used to determine the orientation of particles.

1.8 ± 0.1 g cm^{-3} ($\sim$90% of the theoretical h-BN ρ of $\sim$2.1 g cm^{-3}).[40] We also performed SPS at the same 1700 °C with lower pressure of 45 MPa (for 1 hour), and at maximum achievable high temperature of 2200 °C and 90 MPa pressure (for 30 min) (Fig. S7 and S8, ESI†). Both of the cases show the conversion to h-BN, however, with the signature of lower crystalline quality because the Raman peak intensity is found to be much weaker (Fig. S7 and S8, ESI†) than the 1700 °C and 90 MPa pressure case (Fig. 3). This indicates temperature, in correlation with applied pressure and time plays an important role in c/h-BN formation kinetics. Nevertheless, all of the above observations undeniably confirm the transformation of 3D c-BN to a denser 2D h-BN phase (Fig. 4), when the SPS is performed at elevated temperature.

Regarding the complex BN phase transformations, Solozhenko *et al.*, calculated that c-BN → h-BN conversion occurs at temperatures ranging from $\sim$1000 °C to 1800 °C, driven by the increase in vapor pressure as the temperature rises, owing to an endothermic reaction.[13] Wolfrum *et al.*, demonstrated that low pressure can convert 3D c-BN into 2D h-BN attributed to the presence of potential boron oxide (B_2O_3) impurities acting as catalysts, influencing the phase transformations.[41] Sachdev *et al.*, observed that the grain size of c-BN and the presence of B_2O_3 impact the phase transformation, with the conversion temperature of $\sim$900 °C (for grain size $\sim$1.5 μm) and $\sim$1500 °C (for grain size $\sim$600 μm), thereby affecting the activation kinetics.[42]

In a recent study Cahill *et al.*, investigated the size-dependent transformation of c-BN particles under a helium atmosphere and found that the growth of h-BN depends on both time duration and temperature.[40] Along with the pressure and temperature, it has been argued that grain size and density play a crucial role in the phase transformations.[40,42–44] Arguably, our work is the first experimental observation of pristine c-BN → h-BN phase transformation at elevated temperature ($\geq$ 2000 °C), without any additives (Mg or Si based catalysts) or any B_2O_3 phase (Fig. S9, ESI†).

Regarding the phase transformation mechanism, the current c-BN → h-BN transformation shares a considerable part with the chemically analogous diamond → graphite phase transformation. Graphitization of cubic structures such as diamond and c-BN has long been attracting a consistent interest.[45–47] driven by the industrial relevance, emergence of 2D nanomaterials, and adaptation of new processes like SPS.[48,49] A consensus is reached that the graphitization of cubic diamond powder on a micron scale is a surface energy-driven transformation, transitioning into polycrystalline graphite as the particle size increases.[43,50,51] Such surface energy-driven graphitization is believed to be a rather general phenomena applicable not only to diamond but also to c-BN structure, as h-BN phase is predominantly observed near the surface and grain-interface of c-BN particles.[43] The HTHP conditions cause the crystal structure of c-BN to undergo a phase transition, where the sp^3 hybridized carbon atoms in c-BN are transformed into a sp^2 hybridized structure similar to graphene in h-BN. This phase transition is driven by the reduction of surface energy associated with the formation of the layered h-BN structure. To be noted for a surface-driven phase transformation is that a spontaneous transformation should occur for sub-micron particles when sufficient thermal energy is provided, regardless of the relative stability between the bulk phases.[46] The transformation from the c-BN to the h-BN phase is similar to the graphitization of diamond powder on a micrometer scale, driven by surface energy. It is worth noting that h-BN is commonly found on the surface of c-BN.[40,41] Therefore, simply mechanically grinding 3D c-BN to obtain 2D h-BN may not be sufficient to achieve the desired transformation. Hence, the use of SPS technique is also plays a key role to achieve the transformation from 3D c-BN phase to 2D h-BN phase. Recently, we have also shown that mixed phase c/h-BN transform to h-BN with higher crystalline quality (in comparison with the pristine h-BN), which suggests that c-BN possibly favors the nucleation process of h-BN.[31] Moreover, the high density of the transformed h-BN (1.8 ± 0.1 g cm^{-3}) is also of extreme importance for a wide range of applications. The practical importance of densification of graphitic phase is that it might favor thermo-mechanical properties, critical for applications.[52] Considering the time-consuming multi-step graphite densification processes involved in current industrial practice,[53] SPS might feature a single-step conversion process of dense graphitic material.[48,49]

Thermal conductivity measurement

The thermal conductivity (k) of h-BN is useful for critical temperature management of devices. Therefore, we measured the room temperature k of the fully transformed h-BN by measuring the thermal diffusivity (α) with the laser flash

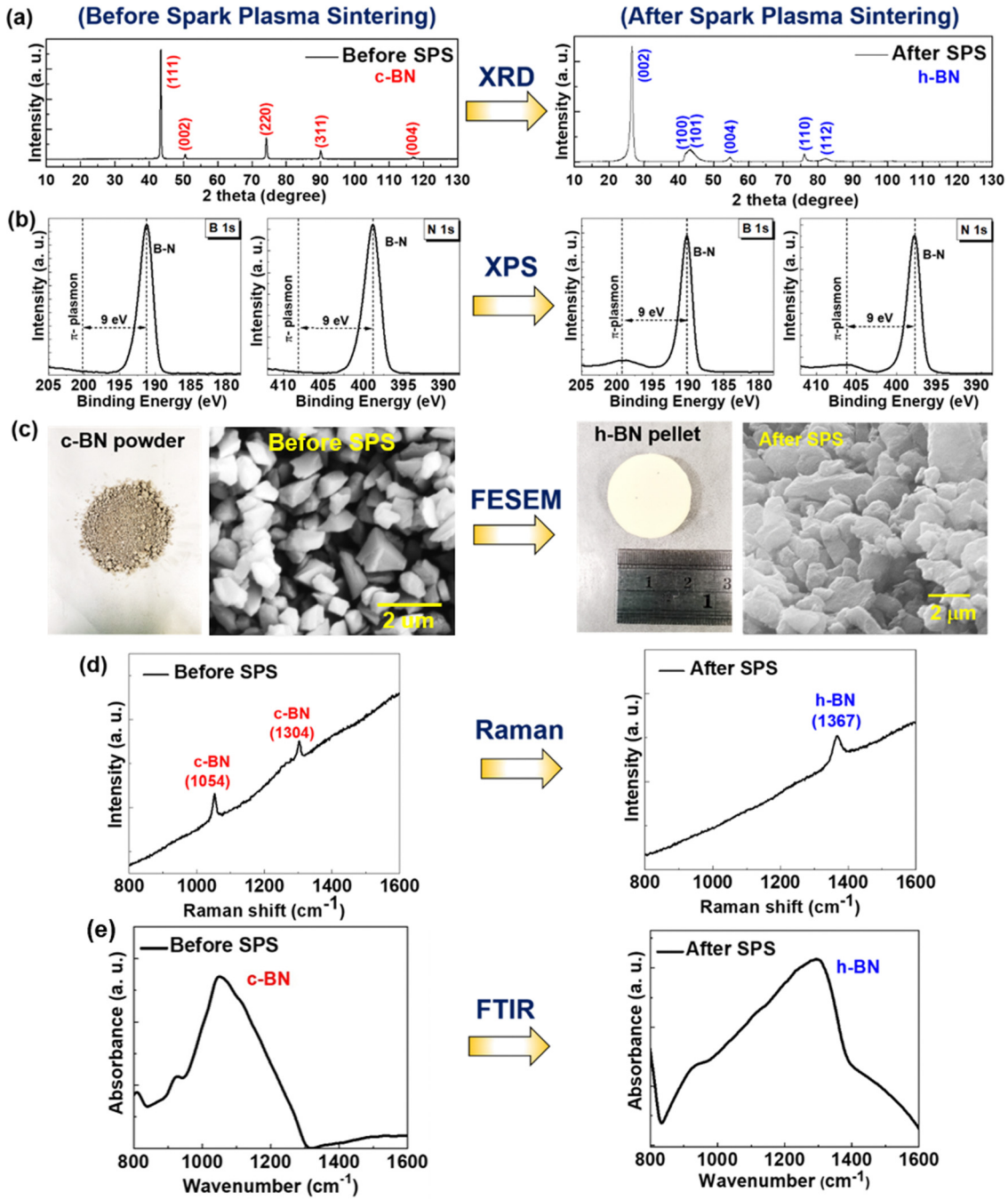

Fig. 3 Characterizations of c-BN, before and after the SPS at 1700 °C, and 90 MPa pressure. (a)–(e) XRD, XPS, FESEM, Raman spectroscopy, and FTIR shows the complete phase transformation of 3D c-BN (left panel) to 2D h-BN (right panel), after the SPS. The as-received c-BN powder and converted h-BN disk is shown (20-mm diameter).

method, the specific heat capacity (C_p) with differential scanning calorimetry (Fig. 5a), the density (ρ) with solid cylinder method, and ultimately by applying the relation $k = C_p \times \rho \times \alpha$. Laser flash method data (temperature rise *vs.* time) were fitted with the Dusza combined model (Fig. 5b).[31,54] We obtained $\alpha = 2.72 \times 10^{-6}$ m^2 s^{-1}, $C_p = 678\ J\ kg^{-1}\ K^{-1}$, yielding $k \sim 3.2 \pm 0.1$ W mK^{-1}. The results are validated by measuring k through two independent h-BN disks (converted from c-BN by SPS), showing similar values (Fig. S10, ESI†). In literature, SPS (at $\geq$ 2000 °C) of pristine h-BN shows k of ~35–280 W mK^{-1}.[55,56] Arguably, ours is the first demonstration of k measurement of phase transformed h-BN. This k value is comparable to the measured pristine h-BN without SPS (Fig. S10, ESI†), as well as with the reported through-plane k_z of bulk h-BN (~2–5 W mK^{-1}).[57–59] The one order difference in k value reported in literature reported SPS h-BN and our SPS processed transformed h-BN might be associated

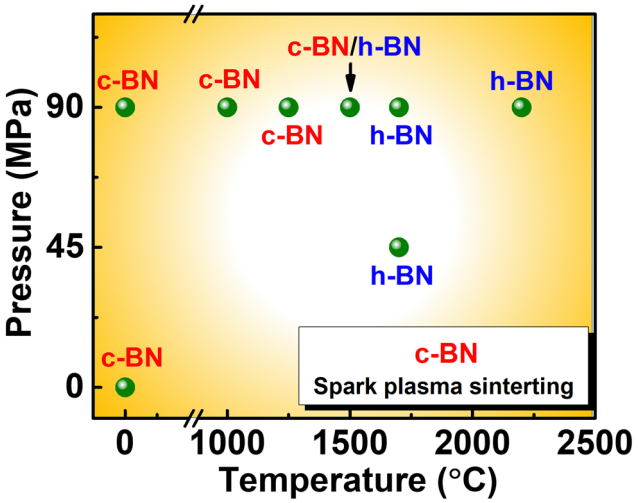

Fig. 4 Phase stability of c-BN. With increasing temperature, phase transformations occur from 3D c-BN to a mixed phase 3D/2D c-BN/h-BN and finally to 2D h-BN.

with the phonon scattering due to random orientations, anisotropic nature of h-BN (in which in-plane shows much higher k value than the cross-plane) and the crystalline quality of h-BN nanosheets.[60] It is important to note that the obtained k value is influenced by the measurement techniques.[61] Specifically, laser flash method, a bulk measurement technique, assesses k including defects, voids, grain boundaries, and flakes oriented in all the random directions (independent of orientations). These are the active-sites for phonon scattering and thus induce possible reduction in the k. Our phase transformed h-BN involves domains with characteristic length in μm-scale. Furthermore, each c-BN particle converts into a polycrystalline h-BN domain, because the surface induced graphitization starts from each facet of c-BN.[43,51] Therefore, each μm-scale domain possibly consists of multiple sub-μm grains due to polycrystallinity. The hierarchical randomness involved in the sub-domain polycrystallinity and the boundaries between μm sized domains may dominate the scattering processes in phonon transport in bulk scale measurement. Nevertheless, k of denser transformed h-BN might be

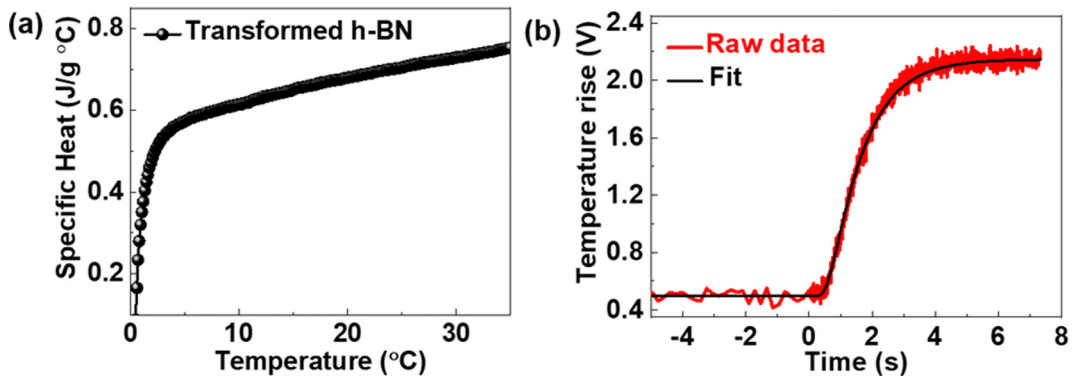

Fig. 5 Specific heat capacity and laser flash method results of phase transformed h-BN. (a) Temperature-dependent specific heat capacity of the phase transformed h-BN determined by the differential scanning calorimetry. (b) Dusza combined model fitting of the laser flash method time-dependent temperature, which was used to determine room temperature thermal conductivity.

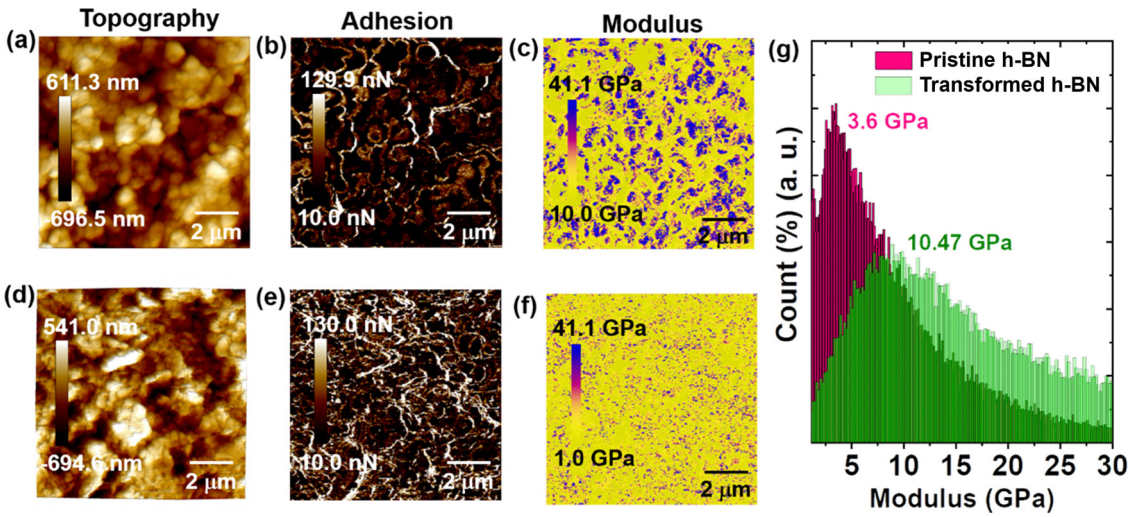

Fig. 6 Nano-mechanical properties of phase transformed (upper panel) and pristine h-BN (lower panel). (a) and (d) Surface topography, (b) and (e) adhesion force map, and (c) and (f) Young's modulus mapping. (g) Gaussian distribution of the Young's modulus of both the h-BN cases.

useful for the tailored thermal conductivity and critical thermal management-related device applications.

Nano-mechanical characterizations

The mechanical elasticity at nanoscale of entirely phase transformed h-BN is measured using atomic force microscopy operated in Peak force tapping mode (see Experimental section). Nanoscale mechanical mapping has been carried out through a stiffer probe (Si covered with native oxide, stiffness 25 N m^{-1}) scanned over an area of 10 × 10 micron over mixed-phase and pristine h-BN at a fixed normal force (400 nN). It is observed that the elastic indentation varies between 3 to 50 nm at different sites of the transformed h-BN (from c-BN) and pristine h-BN. The stiffer regions deformed less than the softer (Fig. S11, ESI†), influencing the contact mechanics as well as surface chemistry (adhesion force values) between the probe and the surface. The Young's modulus values are measured through the contact-mechanical model: Derjaguin, Muller, and Toporov (DMT) and adhesion force values by measuring F–D spectroscopy's retraction part.[62] The topography of transformed h-BN and pristine h-BN disk surface are shown (Fig. 6a and d). Nevertheless, the surface chemistry (distribution of adhesion force values) and localized elasticity distribution are distinguishable. In the transformed h-BN, the number of active sites of adhesion force values are lower than the pristine h-BN, reflecting higher inertness, hardness and hydrophobicity (Fig. 6b and e). The modulus mapping reveals a higher number of stiffer sites (blue in color) in the transformed h-BN as compared with the pristine h-BN (Fig. 6c and f). It is expected that the interfacial regions of the transformed h-BN phase are responsible for higher stiffness regions, which are missing in the pristine h-BN. The histogram distribution of 256 × 256 data points showing the maximum counts values of Young's modulus of transformed h-BN and the as-prepared pristine h-BN ceramic disks are ∼10.47 GPa and ∼3.6 GPa, respectively (Fig. 6g). This three-fold increase in hardness Young's modulus is attributed to the SPS densification process.[44,63]

Conclusion

In conclusion, we explored the stability of c-BN by using the spark plasma sintering at different temperatures. We observed the unique phase transformation from metastable 3D c-BN to mixed phase 3D/2D c-BN/h-BN to finally to most stable 2D h-BN at elevated temperature with a remarkably high ∼90% theoretical density of 2D h-BN. Our findings are important for advancing the fundamental understanding of complex BN phase diagrams and to accelerate in designing novel materials that will survive at the extreme environments of very high temperature. Moreover, thermal and nano-mechanical properties of transformed 2D h-BN hold promise in a wide range of applications, *e.g.* cutting and machining tools, oxidation resistance protecting layers, thermal management and thermal barriers, aerospace and many other extreme environments material based cutting-edge future technology.

Methods

Spark plasma sintering of cubic-boron nitride powder

We used commercially available (99.9% metal basis) c-BN superabrasive mircopowder powders (1 to 2-μm particle size), which were purchased from MSE suppliers (USA). The SPS of in-house sintered pellets was carried out on an SPS 25–10 machine (Thermal Technology LLC, California, USA) at a constant Uniaxial pressing pressure of 45 or 90 MPa and a heating rate of 50 °C min^{-1} (at SPS facility in Texas A-&-M University, USA). The maximum temperature was 2200 °C. Sintering was carried out according to the following scheme: several grams of powder were placed in a graphite mold (20 or 25-mm diameter) and then placed in the sintering chamber under an initial pressure of 5 MPa. It was held at ∼2 × 10^{-5} Torr for ∼30 min, and then sintered for 60 or 30 min under atmospheric pressure of ultra-high purity 5N (∼99.999%) Argon gas medium. The temperature of the SPS process was controlled by an optical pyrometer Raytek (Berlin, Germany) D-13127. After the SPS, pressure was released slowly at ∼5 MPa min^{-1}, whereas the temperature was ramped down at ∼100 °C min^{-1}. For h-BN disk (∼few grams), as-purchased h-BN powder was grounded in an agate mortar and pestle for ∼30 min by adding a few drops of polyvinyl alcohol binder. It was then high pressed (with 4 Ton Load) to make a compact 1-inch diameter disk. The as-made pellet was then sealed inside a quartz tube (in vacuum), and sintered at 1000 °C for 12 h in a box furnace. The ramping up and down rate was ∼100 °C h^{-1}.

Spectroscopic, chemical, and microscopic characterizations (XRD, XPS, FESEM, FTIR, Raman spectroscopy, and HRTEM)

The XRDs were recorded by using the Rigaku SmartLab thin-film X-ray diffractometer (Tokyo, Japan). It was performed at 40 kV and 40 mA, using a monochromatic Cu K_α radiation source (λ = 1.5406 Å) at a scanning rate of 1°/min. XPS was performed by using PHI Quantera SXM scanning X-ray microprobe with a 1486.6 eV monochromatic Al K_α X-ray source. High-resolution core-level elemental B1s and N1s scans were recorded at 26 eV pass energy. FTIR was obtained by using the Nicolet 380 FTIR spectrometer, and a single-crystal diamond window. Renishaw inVia confocal microscope was used for the Raman spectroscopy measurements by using a 532 nm laser as the excitation source. The surface topography was obtained by FESEM (FEI Quanta 400 ESEM FEG). For FESEM, we sputtered ∼10 nm gold on the surface to avoid charging effect.

For the HRTEM, powders from the nanocomposite were dispersed into the isopropyl alcohol solution and sonicated in an ultrasonic bath for 1 hour. The solution was deposited on the TEM grids by the drop-casting method, using pipettes, and left to dry for 30 min. The HRTEM images were obtained *via* aberration corrected Titan Themis^3 (S)TEM at 300 kV accelerating voltage. HRTEM images were smoothed in ImageJ software with a low pass filter, cutting out the higher frequencies in the fast Fourier transformation. Camera length in the diffraction patterns is 185 mm. Diffraction patterns were simulated using the Materials Project website.[64]

Thermal conductivity measurement

The thermal diffusivity of the 1-inch diameter pellets (after the SPS) was measured with the laser flash method by using a Linseis XFA 500 xenon flash thermal conductivity analyzer. A thin layer of graphite spray coating was applied to the surfaces of the pellet to promote laser absorbance. The measurements were conducted at room temperature with a 10 J laser pulse. The density of the pellet was determined by the Archimedes method. The specific heat capacity of the composites was measured utilizing TA instruments differential scanning calorimeter auto 2500. The samples were placed in hermetic aluminum pans, and the specific heat capacity was measured over the temperature range of 0–35 °C at a heating rate of 10 °C min^{-1}.

Nano-mechanical characterizations

Atomic force characterization was performed with a Bruker Dimension Icon placed in the insulation box over the anti-vibrant stage. High-resolution (256 × 256) mechanical mapping was carried out by PeakForce-QNM (Quantitative Nanomechanical Mapping), proprietary Bruker Ltd. The sharp Silicon probe (model: OTEPSA; radii: 20 nm; stiffness: 25 N m^{-1}) was used to investigate the topography simultaneously with adhesion force map and mechanical mapping. All measurements are carried out at room temperature at relative humidity (~35%). The elastic deformation is monitored under a normal force of 400 nN through force–distance (F–D) spectroscopy, where the ''jump to contact'' moment was used to measure elastic properties using the Derjaguin, Muller, and Toporov (DMT) model. The adhesion force map is measured through ''pull-out'' point during the retraction part of F–D curve.

Data availability statement

The data that support the findings of this study are available from the corresponding author upon reasonable request.

Author contributions

A. B., R. V., and P. M. A. conceptualized the study. A. B., C. L., T. G., B. G., J. E. and X. Z. performed the materials characterizations. T. P. and A. B. P. performed the electron microscopy. M. T. and A. D. carried out the nano-mechancial characterizations. G. A. A. and Z. T. measured thermal conductivity. J. L., and A. K. R. helped with phase tranformation analysis. A. G. B., M. R. N., E. J. G., B. B. P., P. D., and T. I. commented on the manuscript. All the authors discussed the results and contributed to the manuscript preparation.

Conflicts of interest

The authors declare that they have no known competing financial interests or personal relationships that could have appeared to influence the work reported in this paper.

Acknowledgements

The authors would like to acknowledge the Spark Plasma Sintering facility at Texas A&M University, TX, USA. P. Dai acknowledges the materials synthesis effort at Rice, supported by the U. S. Department of Energy, Basic Energy Sciences, under Grant No. DE-SC0012311. M. Tripathi and A. B. Dalton from University of Sussex would like to acknowledge the University of Sussex strategic development fund. G. A. Alvarez and Z. Tian acknowledged the use of facilities and instrumentation supported by National Science Foundation through the Cornell University Materials Research Science and Engineering Center DMR-1719875.

The views and conclusions contained in this document are those of the authors and should not be interpreted as representing the official policies, either expressed or implied, of the Army Research Office or the U.S. Government. The U.S. Government is authorized to reproduce and distribute reprints for Government purposes notwithstanding any copyright notation herein.

This work was sponsored in part by the Army Research Office and was accomplished under Cooperative Agreement Number W911NF-19-2-0269. This work was partly sponsored by the Department of the Navy, Office of Naval Research under ONR Award Number N00014-22-1-2357. G. A. Alvarez was sponsored by the National Science Foundation Graduate Research Fellowship under Grant No. 1650114 and by the *GEM* Associate PhD Fellowship.

References

1 V. L. Solozhenko, O. I. Kurakevych and Y. L. Godec, Creation of Nanostuctures by Extreme Conditions: High-Pressure Synthesis of Ultrahard Nanocrystalline Cubic Boron Nitride, *Adv. Mater.*, 2012, **24**, 1540–1544.

2 A. E. Naclerio and P. R. Kidambi, A Review of Scalable Hexagonal Boron Nitride (h-BN) Synthesis for Present and Future Applications, *Adv. Mater.*, 2022, **35**, 2207374.

3 L. Vel, G. Demazeau and J. Etourneau, Cubic boron nitride: synthesis, physicochemical properties and applications, *Mater. Sci. Eng. B*, 1991, **10**, 149.

4 G. Chilkoor, K. Jawaharraj, B. Vemuri, A. Kutana, M. Tripathi, D. Kota, T. Arif, T. Filleter, A. B. Dalton, B. I. Yakobson, M. Meyyappan, M. M. Rahman, P. M. Ajayan and V. Gadhamshetty, Hexagonal Boron Nitride for Sulfur Corrosion Inhibition, *ACS Nano*, 2020, **14**, 14809.

5 A. Biswas, T. Ruan, F. Lee, C. Li, S. A. Iyengar, A. B. Puthirath, X. Zhang, H. Kannan, T. Gray, A. G. Birdwell, M. R. Neupane, P. B. Shah, D. A. Ruzmetov, T. G. Ivanov, R. Vajtai, M. Tripathi, A. Dalton, B. I. Yakobson and P. M. Ajayan, Unidirectional domain growth of hexagonal boron nitride thin films, *Appl. Mater. Today*, 2023, **30**, 101734.

6 S. V. Monteiro, A. L. D. Skury, M. G. de Azavedo and G. S. Bobrovnitchii, Cubic boron nitride competing with diamond as a superhard engineering material – an overview, *J. Mater. Res. Technol.*, 2013, **2**, 68–74.

7 P. B. Mirakami, K. F. McCarty and D. L. Medlin, Review of advances in cubic boron nitride film synthesis, *Mater. Sci. Eng., R*, 1997, **21**, 47–100.
8 C. B. Samantaray and R. N. Singh, Review of synthesis and properties of cubic boron nitride (c-BN) thin films, *Int. Mater. Rev.*, 2005, **50**, 313–344.
9 K. Kádas, G. Kern and J. Hafner, Electronic structure of the (111) and (1−1−1−) surfaces of cubic BN: A local-density-functional ab initio study, *Phys. Rev. B: Condens. Matter Mater. Phys.*, 1999, **60**, 8719.
10 H. Lee, K. Esfarjani, Z. Dong, G. Xiong, A. A. Pelegri and S. D. Tse, Molecular Dynamics Study of Cubic Boron Nitride Nanoparticles: Decomposition with Phase Segregation during Melting, *ACS Nano*, 2016, **10**(11), 10563–10572.
11 F. R. Corrigan and F. P. Bundy, Direct transitions among the allotropic forms of boron nitride at high pressures and temperatures, *J. Chem. Phys.*, 1975, **63**, 3812.
12 K. Albe, Theoretical study of boron nitride modifications at hydrostatic pressures, *Phys. Rev. B: Condens. Matter Mater. Phys.*, 1997, **55**, 6203.
13 V. L. Solozhenko, V. Z. Turkevich and W. B. Holzapfel, Refined Phase Diagram of Boron Nitride, *J. Phys. Chem. B*, 1999, **103**, 2903–2905.
14 V. Z. Turkevich, Phase diagrams and synthesis of cubic boron nitride, *J. Phys.: Condens. Matter*, 2002, **14**, 10963–10968.
15 T. E. Mosuang and J. E. Lowther, Relative stability of cubic and different hexagonal forms of boron nitride, *J. Phys. Chem. Solids*, 2002, **63**, 363–368.
16 W. J. Yu, W. M. Lau, S. P. Chan, Z. F. Liu and Q. Q. Zheng, Ab initio study of phase transformations in boron nitride, *Phys. Rev. B: Condens. Matter Mater. Phys.*, 2013, **67**, 014108.
17 S. Hu, J. Yang, W. Liu, Y. Dong, S. Cao and J. Liu, Prediction of formation of cubic boron nitride by construction of temperature–pressure phase diagram at the nanoscale, *J. Solid State Chem.*, 2011, **184**, 1598.
18 C. Cazorla and T. Gould, Polymorphism of bulk boron nitride, *Sci. Adv.*, 2019, **5**, eaau5832.
19 G. Will, G. Nover and J. von der Gönna, New Experimental Results on the Phase Diagram of Boron Nitride, *J. Solid State Chem.*, 2000, **154**, 280–285.
20 Y. Nikaido, T. Ichibha, K. Hongo, F. A. Roboredo, K. C. Hari Kumar, P. Mahadevan, R. Maezono and K. Nakano, Diffusion Monte Carlo Study on Relative Stabilities of Boron Nitride Polymorphs, *J. Phys. Chem. C*, 2022, **126**(13), 6000–6007.
21 O. Fukunaga, The equilibrium phase boundary between hexagonal and cubic boron nitride, *Diamond Relat. Mater.*, 2000, **9**, 7–12.
22 O. Fukunaga, S. Nakano and T. Taniguchi, Experimental results on the high-pressure phase diagram of boron nitride, *Jpn. J. Appl. Phys.*, 2022, **61**, 125502.
23 D. K. Schreiber, R. Schwaiger, M. Heilmaier and S. J. McCormack, Materials properties characterization in the most extreme environments, *MRS Bull.*, 2022, **47**, 1128.
24 Z. Liu, Y. Gong, W. Zhou, L. Ma, J. Yu, J. C. Idrobo, J. Jung, A. H. MacDonald, R. Vajtai, J. Lou and P. M. Ajayan, Ultrathin high-temperature oxidation-resistant coatings of hexagonal boron nitride, *Nat. Commun.*, 2013, **4**, 2541.
25 C. R. Dean, A. F. Young, I. Meric, C. Lee, L. Wang, S. Songenfrei, K. Watanabe, T. Taniguchi, P. Kim, K. L. Shepard and J. Hone, Boron nitride substrates for high-quality graphene electronics, *Nat. Nano.*, 2010, **5**, 722–726.
26 M. Sajjad and P. Feng, Study the gas sensing properties of boron nitride nanosheets, *Mater. Res. Bull.*, 2014, **49**, 35–38.
27 N. Goel and M. Kumar, Recent advances in ultrathin 2D hexagonal boron nitride based gas sensors, *J. Mater. Chem. C*, 2021, **9**, 1537–1549.
28 A. M. Abrão, D. K. Aspinwall and M. L. H. Wise, in A Review of Polycrystalline Cubic Boron Nitride Cutting tool Developments and Application, ed. Kochhar, A. K., *Proceedings of the Thirtieth International MATADOR Conference*, Palgrave, London, 1993, pp. 169–180, DOI: 10.1007/978-1-349-13255-3_23.
29 S. Guerini, R. H. Miwa, T. M. Schmidt and P. Piquini, Theoretical investigation of the hBN(0001)/cBN(111) interface, *Diamond Relat. Mater.*, 2008, **17**, 1963.
30 Z. Gao, S. Santra, C. R. M. Grovenor and S. C. Speller, Effect of cubic and hexagonal boron nitride additions on the microstructure and properties of bulk MgB_2 superconductors, *Supercond. Sci. Technol.*, 2022, **35**, 084002.
31 A. Biswas, R. Xu, J. Christiansen-Salameh, E. Jeong, G. A. Alvarez, C. Li, A. B. Puthirath, B. Gao, A. Garg, T. Gray, H. Kannan, X. Zhang, J. Elkins, T. S. Pieshkov, R. Vajtai, A. G. Birdwell, M. R. Neupane, B. B. Pate, T. Ivanov, E. J. Garratt, P. Dai, H. Zhu, Z. Tian and P. M. Ajayan, Phase Stability of Hexagonal/cubic Boron Nitride Nanocomposites, *Nano Lett.*, 2023, **23**(15), 6927–6936.
32 W. J. Zhang, Y. M. Chong, I. Bello and S. T. Lee, Nucleation, growth and characterization of cubic boron nitride (cBN) films, *J. Phys. D: Appl. Phys.*, 2007, **40**, 6159–6174.
33 Z. Sun, N. Gao and H. Li, Structural and electronic properties of c-BN (111) surface with hydrogen/fluorine functionalization and nitrogen-based small-molecule adsorption, *J. Phys.: Condens. Matter*, 2020, **32**, 265002.
34 P. Widmayer, H. G. Boyen, P. Ziemann, P. Reinke and P. Oelhafen, Electron spectroscopy on boron nitride thin films: Comparison of near-surface to bulk electronic properties, *Phys. Rev. B: Condens. Matter Mater. Phys.*, 1999, **59**, 5233.
35 T. Werninghaus, J. Hahn, F. Richter and D. R. T. Zahn, Raman spectroscopy investigation of size effects in cubic boron nitride, *Appl. Phys. Lett.*, 1997, **70**, 958–960.
36 S. Saha, A. Rice, A. Ghosh, S. M. N. Hasan, W. You, T. Ma, A. Hunter, L. J. Bissell, R. Bedford, M. Crawford and S. Arafin, Comprehensive characterization and analysis of hexagonal boron nitride on sapphire, *AIP Adv.*, 2021, **11**, 055008.
37 G. Wang, J. Chen, J. Meng, Z. Yin, J. Jiang, Y. Tian, J. Li, J. Wu, P. Jin and X. Zhang, Direct growth of hexagonal boron nitride films on dielectric sapphire substrates by

pulsed laser deposition for optoelectronic applications, *Fundam. Res.*, 2021, **1**, 677–683.
38 J. Narayan and A. Bhaumik, Research Update: Direct conversion of h-BN into pure c-BN at ambient temperatures and pressures in air, *APL Mater.*, 2016, **4**, 020701.
39 J. Y. Jung, J. Kim, Y. Kim, Y. D. Kim, H. Cha, J. Lee, C. Son and D. Hwang, Enhanced Crystallinity and Luminescence Characteristics of Hexagonal Boron Nitride Doped with Cerium Ions According to Tempering Temperatures, *Materials*, 2021, **14**, 193.
40 J. T. Cahill, W. L. Du Frane, C. K. Sio, G. C. S. King, J. C. Soderlind, R. Lu, M. A. Worsley and J. D. Kuntz, Transformation of boron nitride from cubic to hexagonal under 1-atm helium, *Diamond Relat. Mater.*, 2020, **109**, 108078.
41 A. Wolfrum, B. Matthey, A. Michaelis and M. Herrmann, On the Stability of c-BN-Reinforcing Particles in Ceramic Matrix Materials, *Materials*, 2018, **11**, 255.
42 H. Sachdev, R. Haubner, H. Noth and B. Lux, Investigation of the c-BN/h-BN phase transformation at normal pressure, *Diamond Relat. Mater.*, 1997, **6**, 286–292.
43 J. C. Garrett, I. Sigalas, A. K. Wolfrum and M. Herrmann, Effect of cubic boron nitride grain size in the reinforcing of α-Sialonceramics sintered via SPS, *J. Eur. Ceram. Soc.*, 2015, **35**, 451–462.
44 H. Yang, H. Fang, H. Yu, Y. Chen, L. Wang, W. Jiang, Y. Wu and J. Li, Low temperature self-densification of high strength bulk hexagonal boron nitride, *Nat. Commun.*, 2019, **10**, 854.
45 M. Seal, Graphitization of Diamond, *Nature*, 1960, **185**, 522–523.
46 P. Sorokin, A. Kvashnin, Z. Zhu and D. Tomanek, Spontaneous Graphitization of Ultrathin Cubic Structures: A Computational Study, *Nano Lett.*, 2014, **14**(12), 7126–7130.
47 V. Lipp, V. Tkachenko, M. Stransky, B. Aradi, T. Frauenheim and B. Ziaja, Density functional tight binding approach utilized to study X-ray-induced transitions in solid materials, *Sci. Rep.*, 2022, **12**, 1551.
48 R. Alexander, K. Ravikanth, M. Gonal, A. Srivastava and K. Dasgupta, Conversion of diamond polishing powder to high-density isotropic nano-crystalline graphite through spark plasma sintering, *SN Appl. Sci.*, 2020, **2**, 835.
49 J. Aguiar, S. Kwon, B. Coryell, E. Eyerman, A. Bokov, R. Castro, D. Burns, H. Hartmann and E. Luther, Densification of Graphite under High Pressure and Moderate Temperature, *Mater. Today Commun.*, 2020, **22**, 100821.
50 Q. Bai, Z. Wang, Y. Guo, C. Jiaxuan and Y. Shang, Graphitization Behavior of Single Crystal Diamond for the Application in Nano-Metric Cutting, *Curr. Nanosci.*, 2018, **14**, 377–383.
51 J. Qian, C. Pantea, J. Huang, T. W. Zerda and Y. Zhao, Graphitization of diamond powders of different sizes at high pressure–high temperature, *Carbon*, 2004, **42**, 2691–2697.
52 S. Boulfelfel, A. Oganov and S. Leoni, Understanding the nature of ''superhard graphite'', *Sci. Rep.*, 2012, **2**, 471.
53 K. Shen, Z.-H. Huang, K.-X. Hu, W. Shen, S. Yu, J. Yang, Y. Guangzhi and F. Kang, Advantages of natural microcrystalline graphite filler over petroleum coke in isotropic graphite preparation, *Carbon*, 2015, **90**, 197–206.
54 L. Dusza, Combined solution of the simultaneous heat loss and finite pulse corrections with the laser flash method, *HTHP Abstr.*, 1995, **27**, 467–473.
55 J. Xue, J. Liu, B. Xie and G. Zhang, Pressure-induced preferential grain growth, texture development and anisotropic properties of hot pressed hexagonal boron nitride ceramics, *Scr. Mater.*, 2011, **65**, 966–969.
56 S. Mateti, K. Yang, X. Liu, S. Huang, J. Wang, L. H. Li, P. Hodgson, M. Zhou, J. He and Y. Chen, Bulk Hexagonal Boron Nitride with a Quasi-Isotropic Thermal Conductivity, *Adv. Funct. Mater.*, 2018, **28**, 1707556.
57 A. Simpson and A. D. Stuckes, The thermal conductivity of highly oriented pyrolytic boron nitride, *J. Phys. C: Solid State Phys.*, 1971, **4**, 1710.
58 P. Jiang, X. Qian, R. Yang and L. Lindsay, Anisotropic thermal transport in bulk hexagonal boron nitride, *Phys. Rev. Mater.*, 2018, **2**, 064005.
59 C. Yuan, J. Li, L. Lindsay, D. Cherns, J. W. Pomeroy, S. Liu, J. H. Edgar and M. Kubali, Modulating the thermal conductivity in hexagonal boron nitride via controlled boron isotope concentration, *Commun. Phys.*, 2019, **2**, 43.
60 M. T. Alam, M. S. Bresnehan, J. A. Robinson and M. A. Haque, Thermal conductivity of ultra-thin chemical vapor deposited hexagonal boron nitride films, *Appl. Phys. Lett.*, 2014, **104**, 013113.
61 N. Yüksel, The Review of Some Commonly Used Methods and Techniques to Measure the Thermal Conductivity of Insulation Materials, *Insul. Mater. Context Sustainability*, 2016, 113.
62 M. Tripathi, A. King, G. Fratta, M. Meloni, M. Large, J. P. Salvage, N. M. Pugno and A. B. Dalton, Laser-Based Texturing of Graphene to Locally Tune Electrical Potential and Surface Chemistry, *ACS Omega*, 2018, **3**(12), 17000–17009.
63 C. Zou, S. Guo, S. Wang, T. Shen, X. Zhou, B. Li, D. Li and J. Li, Dense additive-free bulk boron nitride ceramics developed by self-densification of borazine, *J. Eur. Ceram.*, 2022, **42**, 2640–2650.
64 A. Jain, S. P. Ong, G. Hautier, W. Chen, W. D. Richards, S. Dacek, S. Cholia, D. Gunter, D. Skinner, G. Ceder and K. A. Persson, Commentary: The Materials Project: A materials genome approach to accelerating materials innovation, *APL Mater.*, 2013, **1**, 011002.

